Subwavelength optical lattices induced by position-dependent dark states

Qingqing Sun,[1] Jörg Evers,[2] Martin Kiffner,[3] and M. Suhail Zubairy[1,2]

[1]*Department of Physics and Astronomy and Institute for Quantum Science and Engineering,*
Texas A&M University, College Station, Texas 77843, USA
[2]*Max-Planck-Institut für Kernphysik, Saupfercheckweg 1, D-69117 Heidelberg, Germany*
[3]*Technische Universität München, Physik-Department I, James-Franck-Straße, D-85748 Garching, Germany*

A method for the generation of subwavelength optical lattices based on multilevel dark states is proposed. The dark state is formed by a suitable combination of standing wave light fields, leading to position-dependent populations of the ground states. An additional field coupling dispersively to one of the ground states translates this position dependence into a subwavelength optical potential. We provide two semiclassical approaches to understand the involved physics, and demonstrate that they lead to identical results in a certain meaningful limit. Then we apply a Monte Carlo simulation technique to study the full quantum dynamics of the subwavelength trapping. Finally, we discuss the relevant time scales for the trapping, optimum conditions, and possible implementations.

I. INTRODUCTION

Light fields are versatile tools for generating optical potentials for the trapping of atoms [1]. In particular, standing wave fields can induce periodic potentials, which is an important method to trap or cool neutral atoms [2,3]. Early experiments have already revealed the possibility of localizing particles to less than one wavelength of the applied trapping field [4–6]. However, *a priori*, the spatial period of the trapping potential of a standing wave field is limited to half the wavelength of the applied wavelength. Due to potential applications such as nanolithography [7], control and enhancement of interactions between the trapped particles, the generation of scatterers for soft x rays, and many others, there has been continuous effort to reduce this periodicity. Gupta and co-workers considered the atomic distribution after traversing an optical field generated by counterpropagating, orthogonally linearly polarized traveling waves [8]. Each magnetic sublevel experiences a light shift. These sublevels are coupled by the multiphoton Raman transition, which provides avoided potential crossing and generates high frequency distribution. Berman and co-workers proposed several high-resolution schemes using coherent transient techniques [9], interference between groups of fields on an optical transition [10] or a Raman transition [11]. Both amplitude and phase gratings can be produced, as well as optical lattices [12]. These techniques are further extended to Fourier-synthesize arbitrary periodic potentials [13,14]. Two-dimensional subwavelength structures have also been realized using radio-frequency dressing [15]. The dressed lattice comprises unit cells whose localized adiabatic eigenstates are spatially varying superpositions of the bare spin states.

In this paper we propose a method for the generation of subwavelength optical lattices. Similar to standard trapping techniques [1], our scheme employs the dispersive coupling of a standing-wave light field S_0 to an optical transition $|g_1\rangle \leftrightarrow |e_0\rangle$ for the generation of a light shift potential, see Fig. 1. In addition, we induce a spatial modulation of the population in the ground state $|g_1\rangle$. This modulation is

achieved via the formation of a position-dependent multilevel dark state in an $N \times \Lambda$ level structure [18] and induced by the application of multiple phase-shifted standing wave light fields. The spatial variation of the effective light shift potential is then determined by the position dependence of S_0 and of the population in the state $|g_1\rangle$. We find that a suitable choice of the standing wave light fields allows us to generate subwavelength trapping potentials. We first provide an intuitive picture for the involved physics based on two semiclassical approaches, which agree in the relevant limiting parameter range. Then, we apply Monte Carlo simulations to study the quantum dynamics of our system, and show that subwavelength trapping potentials are achieved, in agreement with our analytical results.

II. MOTIVATION

Before we turn to the full quantum mechanical simulation in Sec. III, here, we introduce our model system and provide two heuristic approaches which allow us to understand the origin of the subwavelength optical lattice in a simple way. The two models are based on two main assumptions, essentially allowing for a semiclassical treatment: (1) the atoms are sufficiently slow such that they follow the perturbed dark state adiabatically; and (2) the spatial extent of the wave packet is small compared to the optical wavelength.

Our general model system is an $N \times \Lambda$ type system, which consists of the ground states $\{|g_1\rangle, \dots, |g_{N+1}\rangle\}$ and the excited states $\{|e_1\rangle, \dots, |e_N\rangle\}$, as shown in Fig. 1. The dipole allowed transitions in this setup are driven by resonant coupling fields with Rabi frequencies R_n and S_n ($n = 1, \dots, N$), respectively. In addition, the driving field S_0 couples the leftmost ground state $|g_1\rangle$ of the $N \times \Lambda$ system off-resonantly to the excited state $|e_0\rangle$. This field is far detuned by $\Delta = \omega_{\text{atom}} - \omega_{\text{laser}}$, and thereby introduces a light shift potential to the model. A physical realization of the schemes in Fig. 1 is discussed in Sec. V. For each position-dependent Rabi frequency $\Omega(z)$ with $\Omega \in \{S_i, R_i\}$, we denote the maximum value as $\Omega^{(0)}$. Focusing
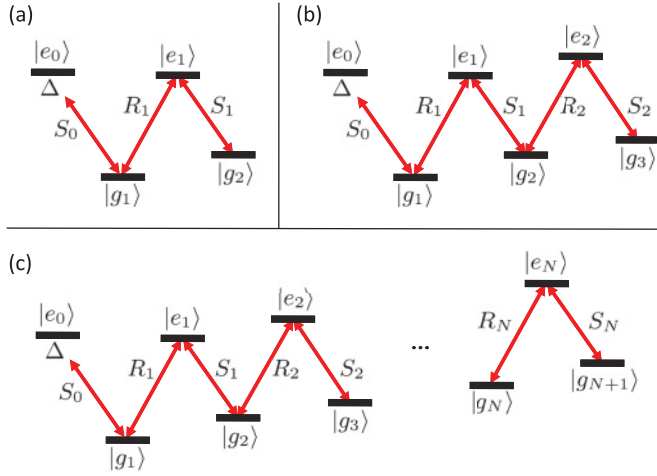
FIG. 1. (Color online) Examples for the level $N \times \Lambda$ structures considered. (a) $1 \times \Lambda$ setup, (b) $2 \times \Lambda$ scheme, and (c) general $N \times \Lambda$ system. Note that in all cases, an off-resonant field S_0 is added to provide a light shift potential.

on a one-dimensional problem in the z direction, the coherent part of the Hamiltonian can thus be written as

$$H_S = \hbar \Delta |e_0\rangle\langle e_0|$$
$$+ \hbar \left[\sum_{n=0}^{N} S_n(z)|e_n\rangle\langle g_{n+1}| + \sum_{n=1}^{N} R_n(z)|e_n\rangle\langle g_n| + \text{H.c.} \right]. \tag{1}$$

The incoherent part will only become relevant in Sec. III. Next we describe two semiclassical approaches for the evaluation of the light shift potential that are based on the Hamiltonian in Eq. (1).

A. Dark state potential approach

The first method follows the idea that the effective light shift potential is the product of the population in state $|g_1\rangle$ and the light shift induced by the field S_0. The $N \times \Lambda$ system alone is known to form a dark state given by [16–18]

$$|D_{N\times\Lambda}\rangle = \frac{\sum_{n=1}^{N+1}(-1)^{n+1}\prod_{k=1}^{n-1}R_k\prod_{j=n}^{N}S_j|g_n\rangle}{\sqrt{\sum_{n=1}^{N+1}\prod_{k=1}^{n-1}|R_k|^2\prod_{j=n}^{N}|S_j|^2}}, \tag{2}$$

where we take the convention $\prod_{k=1}^{0} = \prod_{j=N+1}^{N} = 1$. To simplify the expressions, we introduce the normalization factor

$$\mathcal{N} = \left(\sqrt{\sum_{n=1}^{N+1}\prod_{k=1}^{n-1}|R_k|^2\prod_{j=n}^{N}|S_j|^2} \right)^{-1}. \tag{3}$$

If we assume that the detuning of S_0 is much larger than the corresponding Rabi frequency, $\Delta \gg |S_0^{(0)}|$, this field will introduce a light shift potential, but will only perturb the dark state slightly. In this limit, the total light shift U_N experienced by the atom can be approximated by the light shift that

S_0 would induce in a two-level setting, weighted with the population in $|g_1\rangle$ evaluated from the unperturbed dark state,

$$U_N \cong -\frac{|S_0(z)|^2}{\Delta}|\langle g_1|D_{N\times\Lambda}\rangle|^2. \tag{4}$$

From Eq. (2), we find

$$U_N \cong -\frac{|S_0(z)|^2}{\Delta}\mathcal{N}\prod_{j=1}^{N}|S_j(z)|^2. \tag{5}$$

Note that this result can also be obtained from diagonalizing the system Hamiltonian of Eq. (1) and expanding the eigenvalue λ_N of the dark state to first order in $|S_0^{(0)}|/\Delta$.

B. Dipole force approach

The two semiclassical conditions also allow one to calculate the potential from the dipole forces exerted on the atom by the coupling of the light fields on the different dipole transitions [19]. If an electric field with Cartesian components E_i couples to an atom described by the density operator $\varrho(\vec{r})$, the mean force experienced by the atom is given by

$$\langle \mathbf{F}(\mathbf{r}) \rangle = \sum_{i=1}^{3} \text{Tr}\{\hat{d}_i \varrho(\mathbf{r})\} \nabla E_i(\mathbf{r}), \tag{6}$$

where $\hat{d}_i$ are the components of the electric-dipole moment operator. If the atoms are slow enough, it is justified to evaluate ϱ in the steady state, since the internal degrees of freedom adiabatically follow the change in the experienced field. If we write

$$\mathbf{d} \cdot \mathbf{E} \overset{\text{RWA}}{=} -\hbar \sum_{n=0}^{N}(S_n |e_n\rangle\langle g_{n+1}| + \text{H.c.})$$
$$-\hbar \sum_{n=1}^{N}(R_n |e_n\rangle\langle g_n| + \text{H.c.}), \tag{7}$$

the conservative part of the force can be written as

$$\langle \mathbf{F}(\mathbf{r}) \rangle_{\text{cons}} = -2\hbar \sum_{n=0}^{N} \partial S_n(\mathbf{r})\text{Re}[\langle|e_n\rangle\langle g_{n+1}|\rangle S_n(\mathbf{r})]$$
$$-2\hbar \sum_{n=1}^{N} \partial R_n(\mathbf{r})\text{Re}[\langle|e_n\rangle\langle g_n|\rangle R_n(\mathbf{r})], \tag{8}$$

where mean values $\langle \cdots \rangle$ are evaluated via the steady-state density operator of the internal states for an atom at $\mathbf{r}$. We assumed that all Rabi frequencies are real-valued, which is justified if all fields are standing waves. Running fields with constant amplitude but position-dependent phase contribute to the dissipative force that we neglect here. Furthermore, we introduced the following definitions for the Rabi frequencies $\Omega \in \{S_i, R_i\}$,

$$\partial \Omega(\mathbf{r}) = \frac{1}{\Omega(\mathbf{r})} \nabla \Omega(\mathbf{r}). \tag{9}$$

By integrating the result for the mean force from

$$\langle \mathbf{F}(\mathbf{r}) \rangle_{\text{cons}} = -\nabla U_N(\mathbf{r}), \tag{10}$$

the potential U_N can be obtained. In Appendixes A and B we show that the dipole force approach and Eq. (5) yield equivalent results for a dispersive coupling of S_0 ($|S_0^{(0)}|/\Delta \ll 1$). To this end, we determine the quantum state of the laser-driven atom up to first order in the small parameter $|S_0^{(0)}|/\Delta$ in Appendix A. Based on these results, in Appendix B, we demonstrate that the two semiclassical approaches give identical results in leading order of $|S_0^{(0)}|/\Delta$.

C. Subwavelength potentials

In this section, we discuss possible choices for the laser field configuration leading to subwavelength structures in the potential U_N. These are essentially equivalent for the choices leading to subwavelength lithography [18]. For this, the Rabi frequencies $S_n(z)(0 \leqslant n \leqslant N)$ can be chosen with appropriate relative phases given by

$$S_n(z) = S_n^{(0)}\sin\left[kz + \frac{n\pi}{N+1} + \phi_0\right],\qquad(11)$$

where ϕ_0 is a common phase and k is the effective wave number for all the $S_n(z)$ fields. Note that all standing light waves can have the same wave number k along the trapping axis even if their frequencies are different [18]. This can be achieved if the incident angle of the two plane waves comprising one standing wave is adjusted appropriately with respect to the trapping axis. Moreover, we have shown that a wave-number mismatch corresponding to frequency differences that are small compared to the mean transition frequency is tolerable [18]. Sinusoidal subwavelength structures in the potential U_N require that the normalization constant $\mathcal{N}$ in Eq. (5) is approximately independent of z. This can be achieved by taking all R_n fields to be constant and larger than the corresponding $S_n^{(0)}$, and $R_N \gg S_N^{(0)}$. Then in the normalization factor $\prod_{k=1}^{N}|R_k|^2$ is by far the largest term because all the other terms contain $|S_N|^2$. An important special case is the $1 \times \Lambda$ system, where the choice of $R_1(z) = S_1^{(0)}\sin[kz + \pi + \phi_0]$ does also lead to a position-independent normalization constant $\mathcal{N}$. With these conditions, the potential forms a subwavelength optical lattice with lattice spacing $\lambda/[2(N+1)]$, where $\lambda = 2\pi/k$ is the effective wavelength.

III. QUANTUM MONTE CARLO SIMULATION

We now turn to a calculation of the full quantum dynamics of our model system using a Monte Carlo wave-function method [20]. We take into account the quantum motion of the atom so that we are no longer limited by the semiclassical conditions given in Sec. II. The coherent part of the Hamiltonian can be written as

$$H_Q = \hbar\Delta|e_0\rangle\langle e_0| + \hbar\left[\sum_{n=0}^{N}S_n(Z)|e_n\rangle\langle g_{n+1}|\right.$$
$$\left. + \sum_{n=1}^{N}R_n(Z)|e_n\rangle\langle g_n| + \text{H.c.}\right] + \frac{P^2}{2M},\qquad(12)$$

where M is the mass of the atom chosen as $200\hbar k^2/\Gamma$, and P and Z are the atomic momentum and position operators.

There are two types of relaxations in this system: spontaneous emission and dephasing. The operator C^{ij} corresponds to the spontaneous emission from $|e_i\rangle$ to $|g_j\rangle$. Since only the atomic motion along the z axis is of interest, we take the trace over the other two dimensions and obtain

$$C_{k',q}^{ij} = [\Gamma_{ij}\mathcal{N}_q(k')]^{1/2}\exp(-ik'Z)(\boldsymbol{\epsilon}_q^* \cdot \boldsymbol{\sigma}_{ij}^-),\qquad(13)$$

where Γ_{ij} is the spontaneous emission rate, $\boldsymbol{\epsilon}_q^*(q = 0, \pm 1)$ are the π and circular polarization directions, σ_{ij}^- is the corresponding atomic lowering operator, and $\mathcal{N}_q(k')$ is the normalized probability density for spontaneously emitting a photon with linear momentum $\hbar k'$ and angular momentum $\hbar q$ along the z axis.

To simplify the numerical analysis, we assume for the momentum kicks imposed by the light-matter interaction that all dipole allowed transitions are degenerate, and that only discrete momentum kicks $0, \pm\hbar k$ occur. Correct diffusion rates can nevertheless be obtained by using optimized discrete jump probabilities [20].

The other relaxation type is dephasing, which reduces the coherences but does not change the populations. It can be represented by an operator

$$C_i = \frac{\sqrt{\gamma_{ph}}}{2}[\mathbf{1} - 2|\phi_i\rangle\langle\phi_i|].\qquad(14)$$

where $|\phi_i\rangle$ is any of the $2N + 2$ levels, and we take the identity $\sum_i|\phi_i\rangle\langle\phi_i| = \mathbf{1}$.

The non-Hermitian relaxation Hamiltonian is obtained by adding up all the relaxation channels

$$H_R = -\frac{i\hbar}{2}\left(\sum_{i,j,k',q}C_{k',q}^{ij\dagger}C_{k',q}^{ij} + \sum_i C_i^\dagger C_i\right)$$
$$= -\frac{i\hbar}{2}\left[\Gamma_{01}|e_0\rangle\langle e_0| + \sum_{n=1}^{N}(\Gamma_{nn} + \Gamma_{nn+1})|e_n\rangle\langle e_n| + \frac{\gamma_{ph}}{2}\right].$$
$$\qquad(15)$$

The last term is a constant and can be ignored because it only induces an irrelevant overall phase shift.

In general, the wave function in momentum space can be written as

$$|\phi(t)\rangle = \sum_n\sum_{j=0}^{N}[\alpha_{j+1,n}(t)|g_{j+1}, n\hbar k\rangle + \beta_{j,n}(t)|e_j, n\hbar k\rangle].$$
$$\qquad(16)$$

Following the Monte Carlo procedure, we calculate the jump probabilities for all channels at the beginning of each tiny time step and pick a random number in the range of $(0,1)$. If the random number is larger than the summation of all the probabilities, there is no jump in that time step. So we let the wave function evolve linearly under the action of the non-Hermitian Hamiltonian $H_Q + H_R$. If the random number falls into certain jump region (range equal to its probability), we say that jump occurs and project the corresponding operator to the wave function. In either case we need to normalize the wave function at the end of this time step. Then another time step begins.

We run the evolution interrupted by random jumps many times. Each run gives us a different trajectory of the wave

function. Finally an average over many statistical realizations returns the desired momentum space wave function. The wave function in the position space is then found by Fourier transformation of this momentum distribution.

IV. RESULTS

In all calculations, we assume all Γ_{ij} as equal to the frequency unit Γ, and the dephasing rates are chosen as $10^{-3}\Gamma$. As our first example, we consider the four-level $1 \times \Lambda$ system as shown in Fig. 1(a). The S_n fields are chosen as

$$S_0(z) = S_0^{(0)} \cos(kz), \quad S_1(z) = S_1^{(0)} \sin(kz), \quad (17)$$

whereas for $R_1(z)$ we consider two choices:

$$(a) \quad R_1(z) = S_1^{(0)} \cos(kz), \quad (18a)$$

$$(b) \quad R_1(z) \equiv R_1^{(0)} \gg S_1^{(0)}. \quad (18b)$$

In both cases, the normalization constant $\mathcal{N}$ is (approximately) constant.

We start from the initial wave function $\phi(0) = |g_2, 0\rangle$ so that the atom has to interact with both S_1 and S_0 to reach the additional level and form the coherence. Therefore the subwavelength population pattern appears right from the beginning of the evolution, as shown in Fig. 2.

At the initial moment, the atom has zero momentum and its spatial wave function is uniform across space. Switching on the fields, the atom feels the dipole force and starts to move toward places with lower potential energy. For the fields we choose, the lowest points are located at $kz = \pi/4$ and $3\pi/4$ in a period of π. With time, more and more population is accumulated around these positions. At the same time, part of the initial potential energy is converted to kinetic energy, characterized by p^2. The time scale of this first stage is the time required for the atom to move from the top to the bottom of a potential well. The distance to cross is $\lambda/8$, and the potential depth is $U_{\text{dep}} = \max(U_N)$. In a rough estimation of linear acceleration, we find the time scale

$$t_{\text{dis}} \approx \frac{\lambda}{8}\sqrt{\frac{2M}{U_{\text{dep}}}}. \quad (19)$$

At the end of this stage, the population that moved to the potential minimum begins to climb the other side of the potential well. As a result, the kinetic energy decreases and the population peak gets lower.

Another important factor for the evolution is heating due to scattering or spontaneous emission. Spontaneous emissions can be caused by several mechanisms in our system. The main reason is the residual population in the excited levels arising from a perturbation of the dark state by dephasing and the trapping field S_0. The atom constantly tries to evolve back into the dark state, which leads to the excited state population and light scattering. Another possible reason is the nonadiabatic population transfer when the dark state cannot follow the atom's rapid movement, but our numerical results indicate that for our parameters, this contribution is mostly avoided. The momentum kicks from these processes add additional kinetic energy to the system, such that p^2 constantly increases. With higher kinetic energy, the atom becomes less trapped. So
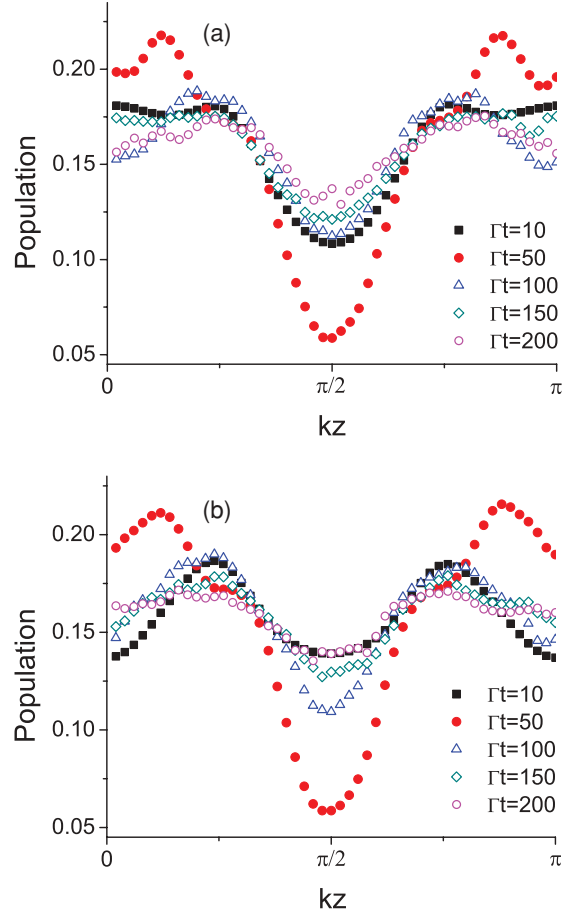
FIG. 2. (Color online) Quantum Monte Carlo results for the position distribution at different times. The parameters are $\Delta = 5$, $S_0 = 2\cos(kz)$, $S_1 = \sin(kz)$, and $R_1 = \cos(kz)$. The results are averaged over 2400 trajectories. In (a), the initial state is $|\phi(0)\rangle = |g_1, 0\rangle$. At short times like $\Gamma t = 10$, there is only one peak in a period of π because only S_0 is involved in the dispersive coupling. In (b), the initial state is $|\phi(0)\rangle = |g_2, 0\rangle$. At $\Gamma t = 10$ there are two peaks because both S_0 and S_1 are required for the dispersive coupling from the initial state. As expected, at later times, the influence of the initial state diminishes.

eventually the lattice structure in the position wave function will be washed out.

To determine the time scale for this washing out, we consider the point at which kinetic energy exceeds the potential depth. For this, we evaluate the heating rate, which depends on the population of the excited levels. We have derived this population to the leading order in $|S_0^{(0)}|/\Delta$, as shown in Appendix A. If the atoms are uniformly distributed in space, the population of the excited levels averaged over a period are

$$\bar{\rho}_{e_0 e_0} \geqslant \frac{S_0^2 S_1^2}{8\Delta^2 R_1^2}, \quad (20a)$$

$$\bar{\rho}_{e_1 e_1} \geqslant \frac{5 S_0^4 S_1^2}{128 \Delta^2 R_1^4}. \quad (20b)$$

The true values for the excited state population should be bigger because the atoms are attracted to regions with

higher values for $S_0^2(z)S_1^2(z)$. Since each emission gives a recoil energy of $2\hbar\omega_r = 2(\hbar^2 k^2/2M)$, the heating rate is

$$2\hbar\omega_r\Gamma\left(\bar{\rho}_{e_0 e_0} + 2\bar{\rho}_{e_1 e_1}\right), \tag{21}$$

where the factor 2 in front of $\bar{\rho}_{e_1 e_1}$ accounts for the two decay channels of level $|e_1\rangle$. This rate is smaller than the value we observed in the simulation. Based exclusively on the recoil heating in Eq. (21), the time scale of washing out can be estimated as

$$t_{\text{wash}} = \frac{U_{\text{dep}}}{2\hbar\omega_r\Gamma\left(\bar{\rho}_{e_0 e_0} + 2\bar{\rho}_{e_1 e_1}\right)}. \tag{22}$$

There are cooling mechanisms to balance this heating effect. For the chosen standing waves with the fixed polarization, Doppler cooling and the blue sideband cooling (if using a negative Δ) occur. For the considered parameters, however, they are not efficient enough to keep the atoms in the shallow potential wells in the steady state. To form a stable optical lattice, external cooling mechanisms would be required. But, if the parameters are chosen carefully, t_{wash} can be sufficiently large such that it does not pose restrictions to typical experimental setups.

Subwavelength lattice potentials can be observed over a large range of parameters, with different properties. A general goal is to achieve high population peaks and long trapping time. When the potential depth is large, the atom is tightly bound to the minima of the potential curve. This leads to high and narrow population peaks as shown in Fig. 3. However, in this case, the heating rate is also relatively high, so the peaks are washed out quickly.
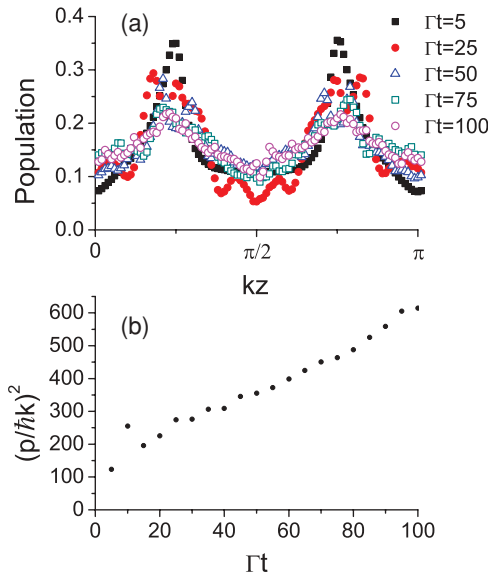
FIG. 3. (Color online) Quantum Monte Carlo results for the position distribution at different times. The parameters are $\Delta = 50$, $S_0 = 20\cos(kz)$, $S_1 = 10\sin(kz)$, and $R_1 = 10\cos(kz)$. All results are averaged over 240 trajectories. Thus, the Rabi frequencies and the detuning are 10 times of those in Fig. 2. (a) shows the position distribution. Since the potential depth is 10 times larger than in Fig. 2, the population peaks are narrower and higher. (b) shows the corresponding kinetic energy. In comparison to Fig. 2, the heating rate is increased by about 6 times.
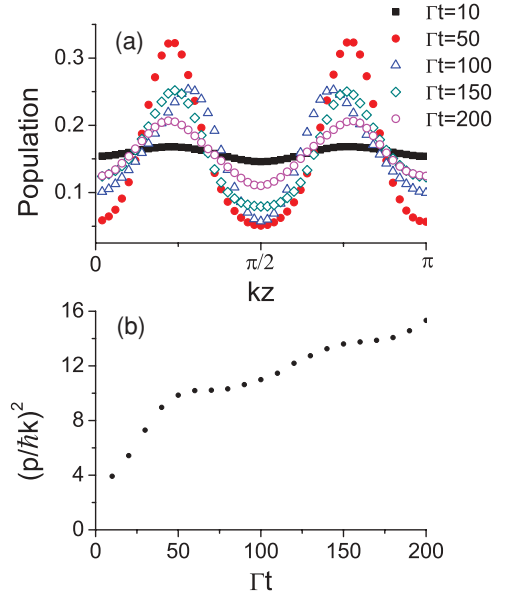
FIG. 4. (Color online) Quantum Monte Carlo results for the position distribution at different times. Parameters are $\Delta = 20$, $S_0 = 2\cos(kz)$, $S_1 = \sin(kz)$, and $R_1 = \cos(kz)$. Results are averaged over 2400 trajectories. The Rabi frequencies are as in Fig. 2, but the detuning is larger. Thus, the potential depth is shallower, and the spontaneous emissions is significantly decreased. As a result, we find smooth and equally distributed position peaks in (a), and a low heating rate in (b).

For larger detunings, the potential depth is smaller due to the inverse relation, but the heating rate decreases further because of the $1/\Delta^2$ dependence. So large detunings are favorable for extended trapping time. With increasing Δ, the population peaks become broader and lower and they persist longer, as shown in Fig. 4.

Another way to reduce the spontaneous emission and thus heating due to scattering is to choose $R_1^{(0)} \gg S_1^{(0)}$. Although the potential wells are then very shallow, the spontaneous emission rate is reduced such that the atoms are trapped for a long time. In fact we observed oscillations in the peak height and p^2 in Fig. 5, which can be interpreted as oscillations of the atom within the potential wells.

To demonstrate that our method also works for higher N, we next consider the six-level $2 \times \Lambda$ system as shown in Fig. 1(b). By choosing the phases of the standing waves as

$$S_0(z) = S_0^{(0)}\sin(kz), \tag{23a}$$

$$S_1(z) = S_1^{(0)}\sin(kz + \pi/3), \tag{23b}$$

$$S_2(z) = S_2^{(0)}\sin(kz + 2\pi/3), \tag{23c}$$

$$R_1(z) = R_1^{(0)}, \quad R_2(z) = R_2^{(0)}, \tag{23d}$$

we find three potential wells within a period of π, as shown in Fig. 6(a). The numerical simulation shows three corresponding population peaks in Fig. 6(b), thus demonstrating subwavelength features of size $\lambda/2(N+1)$. Again we observe the peak-height oscillation due to the atomic oscillation inside the potential wells.
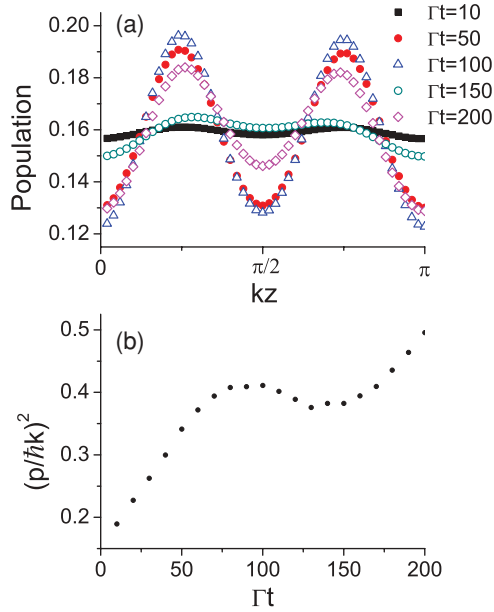
FIG. 5. (Color online) Quantum Monte Carlo results for the position distribution at different times. Parameters are $\Delta = 20$, $S_0 = 2\cos(kz)$, $S_1 = \sin(kz)$, and $R_1 = 3$. Curves are averaged over 2400 trajectories. In (a), we find that the amplitudes of the population peaks oscillate with time. Overall, the trapping time is longer. (b) shows that the heating rate is very small, and the kinetic energy exhibits an oscillatory behavior.

V. PHYSICAL REALIZATION

Here we discuss the realization of our scheme for the generation of subwavelength lattices in atomic systems. In a first step, we discuss the realization of the $1 \times \Lambda$ setup in Fig. 1(a) via the D_1 and D_2 lines in ^{87}Rb [21]. The Λ substructure can be realized via the $^2S_{1/2}(F = 1) \leftrightarrow {}^2P_{1/2}(F = 1)$ transition if circular and orthogonal polarization vectors are chosen for the fields R_1 and S_1, see Fig. 7. A dispersive field S_0 with σ_+ polarization could couple the ground state $|g_1\rangle$ to the $^2P_{3/2}(F = 0)$, $m_F = 0$ state. In addition, one has to take into account that S_0 will also couple $|g_2\rangle$ to states within the $^2P_{3/2}(F = 1,2,3)$ manifolds, see Fig. 7. This coupling is unwanted and can be minimized if the splitting between the ground states $|g_1\rangle$ and $|g_2\rangle$ is large enough such that $|\Delta + \delta_g| \gg |\Delta|$. In practice, this condition can be achieved via the application of an external magnetic field. Note that the $^2P_{3/2}(F = 0)$, $m_F = 0$ state remains energetically lower than the $^2P_{3/2}(F = 1,2,3)$ manifolds in the presence of a magnetic field [21]. Furthermore, the field S_0 will couple dispersively to the transition $|g_1\rangle \leftrightarrow |e_1\rangle$ with detuning δ_{12}. This coupling gives rise to an additional force that has to be small compared to the wanted contribution arising from the resonant field R_1. However, this is indeed the case since the detuning δ_{12} is extremely large (of the order of 7 THz) in the considered example. In order to verify these considerations, we performed numerical calculations based on the dipole force approach in Sec. II B and for the parameters of Fig. 4. The result is shown in Fig. 7(b), where the solid black line denotes the light shift potential including the unwanted couplings induced by S_0 [dashed lines in Fig. 1(a)]. This solid line was obtained by averaging the resulting potential in time over a period that is
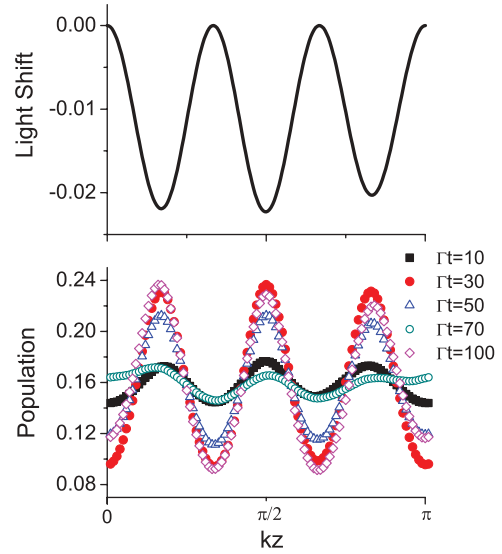
FIG. 6. (Color online) Quantum Monte Carlo results for the position distribution at different times for a $2 \times \Lambda$ 6-level setup. Parameters are $\Delta = 30$, $S_0 = 10\sin(kz)$, $S_1 = 5\sin(kz + \pi/3)$, $S_2 = 5\sin(kz + 2\pi/3)$, $R_1 = 5$, and $R_2 = 15$. The results are averaged over 1200 trajectories. (a) Theoretical expectation for the the light-induced potential from our analytical results for the 6-level system. Compared to the 4-level system, a higher subwavelength resolution is achieved. (b) The corresponding population distribution obtained from the Monte Carlo simulation. Again, the peak heights oscillate with time.

larger than $1/\delta_g$ but much smaller than $1/\Gamma$. The potential clearly exhibits two potential minima within an interval $\lambda/2$, and therefore the desired subwavelength structure. The dashed red line in Fig. 7(b) denotes the expected light shift according to Eq. (5). Note that the deviations between the solid and the dashed line are caused primarily by higher order terms in $1/\Delta$ that were excluded in the simple model leading to Eq. (5). On the other hand, the influence of the unwanted couplings induced by S_0 is negligible.

Next we discuss an alternative way for the realization of the $1 \times \Lambda$ system that does not employ the polarization of the fields. This approach requires that the frequencies of the various transitions are sufficiently distinct such that they can be addressed individually. Dipole transitions with unique frequencies can be found in atomic systems where a magnetic field induces different Zeeman shifts in two angular momentum multiplets, see Fig. 7. Alternatively, one could employ the $F = 1$ and $F = 2$ manifolds of the $^2S_{1/2}$ state for the ground states of the Λ substructure, and $|g_1\rangle$ is represented by the $^2P_{1/2}$, $F = 1$ manifold. This setup exhibits a larger frequency difference δ_g and would allow one to increase $|\Delta|$ and the Rabi frequency S_0 of the dispersive field, and therefore the depth of the trapping potential. The addressing of transitions via their frequency bears the disadvantage that R_1 will couple dispersively to the transition that is resonantly driven by S_1 and vice versa. This coupling gives rise to additional forces that have to be small compared to the wanted contribution arising from the resonantly driven transition. We have performed proof-of-principle numerical simulations in the system shown in Fig. 7(a) that include the unwanted coupling of R_1 (S_1) to the transition $|g_2\rangle \leftrightarrow |e_1\rangle$ ($|g_1\rangle \leftrightarrow |e_1\rangle$). If the resulting
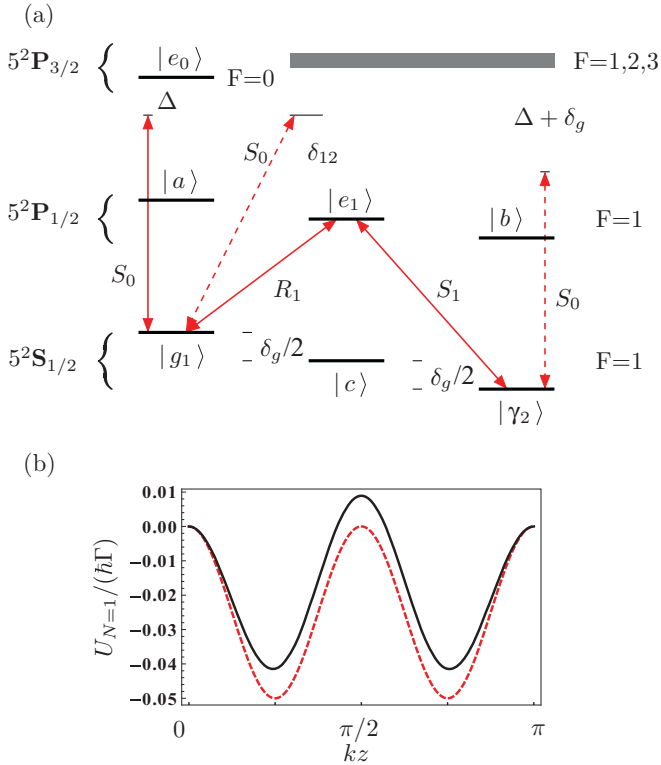
FIG. 7. (Color online) (a) Potential realization of the 4-level $1 \times \Lambda$-system in Fig. 1(a) via atomic states of the D_1 and D_2 line in ^{87}Rb. The states $|g_1\rangle$, $|g_2\rangle$ and $|e_1\rangle$ correspond to magnetic quantum numbers $m_F = -1, 1, 0$, respectively. Note that the transition $(F = 1, m_F = 0) \leftrightarrow (F' = 1, m_F = 0)$ is dipole forbidden. All standing light fields and the magnetic field are applied along the trapping axis z. (b) Calculated light shift potential for the parameters of Fig. 4. The red dashed line represents the light shift potential according to Eq. (5). The solid black line corresponds to a numerical calculation via the dipole force approach [see Sec. II B] and includes the unwanted couplings of S_0 to additional transitions.

potential is averaged in time over a period that is larger than $1/\delta_g$ but much smaller than $1/\Gamma$, we again obtain the black curve in Fig. 7(b). It follows that our scheme can be realized even if individual transitions cannot be addressed by their polarization.

The realization of the general $N \times \Lambda$ level configuration requires that each transition can be addressed individually via its frequency. Furthermore, a realization of our scheme must take into account that the dispersive field S_0 will, in general, couple to other ground states than $|g_1\rangle$. It follows that the detuning Δ of the dispersive coupling and the level structure of the ground and excited states must be chosen such that the transition $|g_1\rangle \leftrightarrow |e_0\rangle$ gives the dominant contribution.

VI. SUMMARY AND DISCUSSION

In summary, we propose a scheme to achieve subwavelength optical lattices. It is based on a position-dependent dark state, achieved by a set of resonant position-dependent driving fields. In addition, a single field is coupled dispersively to one of the ground states of the system, translating the dark state population distribution into an effective optical potential.

Limitations to our scheme are essentially given by processes which perturb the atoms out of the dark state, which are either scattering processes, dephasing processes, or the trapping field itself. For suitable parameters, the system essentially remains in the dark state, such that the lattice is stable over an extended time period. Note that a given setup allows one to dynamically adjust the lattice period to lower values by turning on or off the driving fields on the right side of the level scheme, thus effectively changing the order N of the $N \times \Lambda$ level scheme.

Our scheme can be realized in realistic atomic systems. In particular, we discuss a potential realization of the $1 \times \Lambda$ system in ^{87}Rb. The required transitions are addressed via a combination of frequency and polarization selection. Numerical calculations indicate that the inevitable coupling of the applied light fields to unwanted transitions can be negligible, provided that the frequency differences of the involved transitions are sufficiently large. Unique transition frequencies can be achieved by the application of a magnetic field, giving rise to different Zeeman shifts of angular momentum multiplets. Alternatively, one could employ transitions between different electronic levels giving rise to even larger frequency differences. Furthermore, we verified numerically that the $1 \times \Lambda$ system could be realized with frequency selection only. This opens up the possibility of realizing the general $N \times \Lambda$ schemes.

APPENDIX A: DERIVATION OF THE SEMICLASSICAL STEADY STATE

The unperturbed dark state provides the approximation for the ground-state coefficients in zeroth order of the expansion $|S_0^{(0)}|/\Delta$:

$$|D_{N \times \Lambda}\rangle = \frac{\sum_{n=1}^{N+1}(-1)^{n+1}\prod_{k=1}^{n-1}R_k \prod_{j=n}^{N}S_j|g_n\rangle}{\sqrt{\sum_{n=1}^{N+1}\prod_{k=1}^{n-1}R_k^2 \prod_{j=n}^{N}S_j^2}}. \quad (A1)$$

The perturbed dark state in the leading order of $|S_0^{(0)}|/\Delta$ can be written as

$$|D'_{N \times \Lambda}\rangle = c_{e_0}|e_0\rangle + \cdots + c_{e_N}|e_N\rangle + |D_{N \times \Lambda}\rangle. \quad (A2)$$

Since it is an eigenstate, we have

$$H_S|D'_{N \times \Lambda}\rangle = \hbar\lambda_N|D'_{N \times \Lambda}\rangle, \quad (A3)$$

with the eigenvalue

$$\lambda_N = -\mathcal{N}^2 \frac{S_0^2}{\Delta}\prod_{i=1}^{N}S_i^2. \quad (A4)$$

By examining the coefficients of the state $|e_0\rangle$ on both sides of Eq. (A3), we obtain

$$\hbar\Delta c_{e_0} + \hbar S_0 c_{g_1} = \hbar\lambda_N c_{e_0}. \quad \text{(A5)}$$

Since $\lambda_N \ll \Delta$, in the leading order

$$c_{e_0} \approx -\frac{S_0}{\Delta}c_{g_1} = -\frac{S_0}{\Delta}\mathcal{N}\prod_{i=1}^{N}S_i. \quad \text{(A6)}$$

Continuing with the coefficients for $|g_1\rangle$ we obtain

$$\hbar S_0 c_{e_0} + \hbar R_1 c_{e_1} = \hbar\lambda_N c_{g_1}, \quad \text{(A7)}$$

which can be written as

$$c_{e_1} = \frac{\lambda_N}{R_1}c_{g_1} - \frac{S_0}{R_1}c_{e_0}. \quad \text{(A8)}$$

This procedure leads to a recursive relation

$$c_{e_n} = \frac{\lambda_N}{R_n}c_{g_n} - \frac{S_{n-1}}{R_n}c_{e_{n-1}}, \quad \text{(A9)}$$

for $1 \leqslant n \leqslant N$. After iteration it becomes

$$c_{e_n} = \frac{\lambda_N}{R_n}c_{g_n} - \frac{S_{n-1}}{R_n}\left(\frac{\lambda_N}{R_{n-1}}c_{g_{n-1}} - \frac{S_{n-2}}{R_{n-1}}c_{e_{n-2}}\right), \quad \text{(A10)}$$

which can be evaluated as

$$c_{e_n} = \frac{\lambda_N}{R_n}\sum_{j=0}^{n-1}(-1)^j\prod_{i=1}^{j}\frac{S_{n-i}}{R_{n-i}}c_{g_{n-j}} + (-1)^n\prod_{j=0}^{n-1}\frac{S_j}{R_{j+1}}c_{e_0}.$$

Substituting in the known coefficients in the above equations leads finally to the compact form for the excited levels

$$c_{e_n} = \frac{(-1)^n\mathcal{N}\lambda_N}{R_n\prod_{k=1}^{n-1}R_k\prod_{l=n}^{N}S_l}\sum_{j=n+1}^{N+1}\prod_{k=1}^{j-1}R_k^2\prod_{l=j}^{N}S_l^2. \quad \text{(A11)}$$

As an example, we consider $n = N$ in Eq. (A11) and find

$$c_{e_N} = \frac{(-1)^N\mathcal{N}\lambda_N}{S_N}\prod_{k=1}^{N}R_k. \quad \text{(A12)}$$

Comparing this to the result obtained directly from the coefficients of $|g_{N+1}\rangle$,

$$\hbar S_N c_{e_N} = \hbar\lambda_N c_{g_{N+1}}, \quad \text{(A13)}$$

we find identical results.

APPENDIX B: EQUIVALENCE OF THE TWO SEMICLASSICAL APPROACHES

In this appendix, we demonstrate that the two semiclassical methods presented in Sec. II lead to identical results in the leading order of the expansion $|S_0^{(0)}|/\Delta$.

In the dark-state potential method, the force can be found by taking the derivative of the potential energy.

$$\langle\mathbf{F}\rangle = -\nabla\lambda_N = \nabla\left(\frac{\mathcal{N}^2}{\Delta}S_0^2\prod_{i=1}^{N}S_i^2\right)$$

$$= \sum_{\Omega}\frac{d}{d\Omega}\left(\frac{\mathcal{N}^2}{\Delta}S_0^2\prod_{i=1}^{N}S_i^2\right)\nabla\Omega. \quad \text{(B1)}$$

The terms for fields S_0, S_n, R_n are

$$\frac{d}{dS_0}\left(\frac{\mathcal{N}^2}{\Delta}S_0^2\prod_{i=1}^{N}S_i^2\right)\nabla S_0 = \frac{2\mathcal{N}^2 S_0}{\Delta}\prod_{i=1}^{N}S_i^2\nabla S_0, \quad \text{(B2)}$$

$$\frac{d}{dS_n}\left(\frac{\mathcal{N}^2}{\Delta}S_0^2\prod_{i=1}^{N}S_i^2\right)\nabla S_n$$

$$= -\frac{2\lambda_N}{S_n}\nabla S_n + \lambda_N\mathcal{N}^2\frac{d}{dS_n}\left(\sum_{j=1}^{N+1}\prod_{k=1}^{j-1}R_k^2\prod_{l=j}^{N}S_l^2\right)\nabla S_n$$

$$= -2\lambda_N\mathcal{N}^2\sum_{j=n+1}^{N+1}\prod_{k=1}^{j-1}R_k^2\prod_{l=j}^{N}S_l^2\frac{\nabla S_n}{S_n}, \quad \text{(B3)}$$

$$\frac{d}{dR_n}\left(\frac{\mathcal{N}^2}{\Delta}S_0^2\prod_{i=1}^{N}S_i^2\right)\nabla R_n$$

$$= \lambda_N\mathcal{N}^2\frac{d}{dR_n}\left(\sum_{j=1}^{N+1}\prod_{k=1}^{j-1}R_k^2\prod_{l=j}^{N}S_l^2\right)\nabla R_n$$

$$= 2\lambda_N\mathcal{N}^2\sum_{j=n+1}^{N+1}\prod_{k=1}^{j-1}R_k^2\prod_{l=j}^{N}S_l^2\frac{\nabla R_n}{R_n}. \quad \text{(B4)}$$

To find the force using the dipole force method, we will borrow some results from the first method. Namely, the coefficients from Appendix A lead to the coherence - nondiagonal density matrix elements. The dipole force can be written as

$$\langle\mathbf{F}\rangle = -2\sum_{\Omega}\frac{\nabla\Omega}{\Omega}\text{Re}\left[\rho_{eg}^{(\Omega)}\Omega\right] = -2\sum_{\Omega}c_e c_g^*\nabla\Omega. \quad \text{(B5)}$$

The force contribution due to S_0, S_n, and R_n are

$$-2c_{e_0}c_{g_1}^*\nabla S_0 = 2\frac{S_0}{\Delta}|c_{g_1}|^2\nabla S_0 = \frac{2S_0}{\Delta}\mathcal{N}^2\prod_{i=1}^{N}S_i^2\nabla S_0, \quad \text{(B6)}$$

$$-2c_{e_n}c_{g_{n+1}}^*\nabla S_n = -2\lambda_N\mathcal{N}^2\sum_{j=n+1}^{N+1}\prod_{k=1}^{j-1}R_k^2\prod_{l=j}^{N}S_l^2\frac{\nabla S_n}{S_n}, \quad \text{(B7)}$$

$$-2c_{e_n}c_{g_n}^*\nabla R_n = 2\lambda_N\mathcal{N}^2\sum_{j=n+1}^{N+1}\prod_{k=1}^{j-1}R_k^2\prod_{l=j}^{N}S_l^2\frac{\nabla R_n}{R_n}. \quad \text{(B8)}$$

These results agree exactly with those from the dark-state potential method.

[1] H. J. Metcalf and P. van der Straten, *Laser Cooling and Trapping* (Springer, New York, 1999).

[2] P. S. Jessen and I. H. Deutsch, Adv. At. Mol. Opt. Phys. **37**, 95 (1996).

[3] G. Grynberg and C. Robilliard, Phys. Rep. **355**, 335 (2001).

[4] C. I. Westbrook, R. N. Watts, C. E. Tanner, S. L. Rolston, W. D. Phillips, P. D. Lett, and P. L. Gould, Phys. Rev. Lett. **65**, 33 (1990).

[5] P. Verkerk, B. Lounis, C. Salomon, C. Cohen-Tannoudji, J.-Y. Courtois, and G. Grynberg, Phys. Rev. Lett. **68**, 3861 (1992).

[6] P. S. Jessen, C. Gerz, P. D. Lett, W. D. Phillips, S. L. Rolston, R. J. C. Spreeuw, and C. I. Westbrook, Phys. Rev. Lett. **69**, 49 (1992).

[7] Th. Schulze, B. Brezger, R. Mertens, M. Pivk, T. Pfau, and J. Mlynek, Appl. Phys. B **70**, 671 (2000).

[8] R. Gupta, J. J. McClelland, P. Marte, and R. J. Celotta, Phys. Rev. Lett. **76**, 4689 (1996).

[9] B. Dubetsky and P. R. Berman, Phys. Rev. A **50**, 4057 (1994).

[10] P. R. Berman, B. Dubetsky, and J. L. Cohen, Phys. Rev. A **58**, 4801 (1998).

[11] B. Dubetsky and P. R. Berman, Laser Phys. **12**, 1161 (2002).

[12] R. Zhang, N. V. Morrow, P. R. Berman, and G. Raithel, Phys. Rev. A **72**, 043409 (2005).

[13] M. Weitz, G. Cennini, G. Ritt, and C. Geckeler, Phys. Rev. A **70**, 043414 (2004).

[14] G. Ritt, C. Geckeler, T. Salger, G. Cennini, and M. Weitz, Phys. Rev. A **74**, 063622 (2006).

[15] N. Lundblad, P. J. Lee, I. B. Spielman, B. L. Brown, W. D. Phillips, and J. V. Porto, Phys. Rev. Lett. **100**, 150401 (2008).

[16] M. S. Zubairy, A. B. Matsko, and M. O. Scully, Phys. Rev. A **65**, 043804 (2002).

[17] A. B. Matsko, I. Novikova, M. S. Zubairy, and G. R. Welch, Phys. Rev. A **67**, 043805 (2003).

[18] M. Kiffner, J. Evers, and M. S. Zubairy, Phys. Rev. Lett. **100**, 073602 (2008).

[19] C. Cohen-Tannoudji, J. Dupont-Roc, and G. Grynberg, *Atom-Photon Interactions: Basic Processes and Applications* (Wiley, New York, 1992).

[20] K. Mølmer, Y. Castin, and J. Dalibard, J. Opt. Soc. Am. B **10**, 524 (1993).

[21] D. A. Steck, Rubidium 87 D line data [http://steck.us/alkalidata/].